



# Effect of Microstructure Evolution of Iron-Rich Intermetallic Compounds on Mechanical Property of Al–7Si–0.3Mg Casting Alloy with Low Iron Content

JIANHUA ZHAO, YU GUO, BEI XU, CHENG GU, YAJUN WANG, and QI TANG

In this study, the effects of microstructure evolution of iron-rich intermetallic compounds on mechanical properties in Al–7Si–0.3Mg cast alloys with low iron content (0.1 to 0.3 wt pct) were investigated. A series of characterization methods was utilized to observe the microstructure of iron-rich intermetallic compounds. The results indicate that the dominant iron-rich intermetallic compounds change from  $\pi$ -AlMgFeSi phase with a script-like morphology to  $\beta$ -AlFeSi phase with a needle-like morphology as Fe content increased. Besides, the 2D/3D morphology of Fe-rich intermetallic compounds significantly changes with the increase of Fe content. In 0.3 wt pct Fe alloy, the  $\pi$ -AlMgFeSi phase with a layered structure and seaweed-like morphology forms on the surface of the  $\beta$ -AlFeSi phase with a platelet-like morphology, and the crystallographic orientation relationships were  $[1100]_{\pi} \parallel [111]_{\beta}$  and  $(\bar{1}10)_{\beta} \parallel (1\bar{2}10)_{\pi}$ . In addition, the  $\beta$ -AlFeSi phase tends to nucleate in 0.2 wt pct Fe alloy, while the growth of  $\beta$ -AlFeSi phase is boosted in 0.3 wt pct Fe alloy. The sufficient growth of  $\beta$ -AlFeSi phase leads to the formation of the  $\pi$ -AlMgFeSi phase. Furthermore, the formation of the  $\pi$ -AlMgFeSi phase improves the mechanical properties of alloys. The microstructure morphology of  $\pi$ -AlMgFeSi phase formed on the surface of the platelet-like  $\beta$ -AlFeSi phase enhances the adhesive strength between the  $\beta$ -AlFeSi and the matrix and reduces the negative effects of Fe-rich intermetallic compounds on mechanical properties of Al–7Si–0.3Mg cast alloys.

<https://doi.org/10.1007/s11663-021-02390-5>

© The Minerals, Metals & Materials Society and ASM International 2021

## I. INTRODUCTION

AL–SI–MG alloys, such as A356 alloy, have been widely used in automotive and aerospace industries because of the excellent castability and mechanical properties.<sup>[1]</sup> Iron (Fe), as one of the common impurities, is often introduced into Al–Si–Mg alloys unintentionally and inevitably during the smelting process, which directly reduces the mechanical properties, the corrosion resistance, and the machinability of the products.<sup>[2]</sup> Owing to the low equilibrium solubility of Fe in solid Al, Fe-rich intermetallic compounds are formed during solidification, such as  $\alpha$ -AlFeSi ( $\alpha$ -Al<sub>8</sub>Fe<sub>2</sub>Si, hexagonal:  $a = 1.23$  nm,  $c = 2.63$  nm),

$\beta$ -AlFeSi ( $\beta$ -Al<sub>5</sub>FeSi or  $\beta$ -Al<sub>4.5</sub>FeSi, monoclinic:  $a = 0.5792$  nm,  $b = 1.2273$  nm,  $c = 0.4313$  nm,  $\beta = 98.93$  deg, or  $a = b = 0.618$  nm,  $c = 2.08$  nm,  $\beta = 91$  deg), and  $\pi$ -AlMgFeSi ( $\pi$ -Al<sub>8</sub>Mg<sub>3</sub>FeSi<sub>6</sub> or  $\pi$ -Al<sub>6</sub>Mg<sub>3</sub>FeSi<sub>5</sub>, hexagonal:  $a = 0.663$  nm,  $c = 0.794$  nm).<sup>[3,4]</sup> The hard and brittle intermetallic compounds not only act as crack initiation sites, but also provide further crack propagation paths in Al–Si–Mg alloys.<sup>[5]</sup>

Most Fe-rich intermetallic compounds appear as needles or platelets in the microstructure of Al–Si–Mg alloys. It is found that Fe-rich intermetallic compounds tend to form the needle-like  $\beta$ -AlFeSi phase instead of the  $\alpha$ -AlFeSi phase when the Fe content<sup>[4]</sup> or the cooling rate is low.<sup>[6]</sup> Many studies have been performed to transform the  $\beta$ -AlFeSi phase to another phase or alter the morphology of  $\beta$ -AlFeSi phase, aiming at improving mechanical properties of alloy.<sup>[7,8]</sup> A traditional method is to add the neutralized elements into the melt,<sup>[9–12]</sup> such as Mn, Cr, Co, Be, Mo, Re, *etc.* However, these methods cannot reduce the Fe content directly. In addition, the excessive neutralized elements may result in solute segregation and reduce mechanical properties of the alloy eventually. On the other hand, the processing parameters, including melt undercooling, cooling rate, and so on, are associated with the formation of Fe-rich intermetallic compounds. Narayanan *et al.*<sup>[13]</sup>

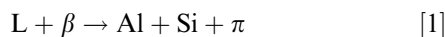
JIANHUA ZHAO is with the College of Materials Science and Engineering, Chongqing University, Chongqing 400045, China and also with the State Key Laboratory of Mechanical Transmission, Chongqing University, Chongqing 400044, China. YU GUO, BEI XU, CHENG GU, YAJUN WANG, and QI TANG are with the College of Materials Science and Engineering, Chongqing University. Contact e-mail: gucheng.90@cqu.edu.cn

Manuscript submitted August 30, 2021; accepted November 11, 2021.

Article published online January 8, 2022.

performed nonequilibrium heat treatment and modified the morphology of  $\beta$ -AlFeSi phase from needle-like into globular when the solution treatment temperature was 788 K to 793 K (515 °C to 520 °C). Although the high solution temperature can change the morphology of  $\beta$ -AlFeSi phase without neutralized elements, the excessive temperature may form liquid phases and result in surface oxidation and surface irregularities. Liu *et al.*<sup>[14]</sup> observed the morphology of Fe-rich intermetallic compounds of Al alloy produced by high pressure die casting. No  $\beta$ -AlFeSi phase was found with the high cooling rate in high pressure die cast Al alloy, while  $\alpha$ -AlFeSi phase was the majority intermetallic compound. Wagner *et al.*<sup>[15]</sup> investigated the influence of melt conditioning and filtration on Fe-rich phase in Al alloy. They found that by sedimentation and subsequent filtration, the Fe content and the formation of brittle  $\beta$ -Al<sub>4.5</sub>FeSi phase can be reduced.

Another Fe-rich intermetallic compound is the  $\pi$ -AlMgFeSi phase, which mainly has a Chinese-script shape. Foss *et al.*<sup>[16,17]</sup> studied the  $\pi$ -Al<sub>9</sub>Mg<sub>3</sub>FeSi<sub>5</sub> phase by electron channeling and symmetry-and-site-sensitive electron microscope techniques. Krendelsberger *et al.*<sup>[18]</sup> obtained the lattice parameters of  $\pi$ -Al<sub>9</sub>Mg<sub>3</sub>FeSi<sub>5</sub> phase (hexagonal:  $a = 0.6625$  nm,  $c = 0.7910$  nm) and studied the characteristics of  $\pi$ -Al<sub>9</sub>Mg<sub>3</sub>FeSi<sub>5</sub> phase. Wang and Davidson<sup>[19]</sup> found that the  $\pi$ -AlMgFeSi phase releases the element Mg during solution treatment and then transforms to another phase. Besides, the increase of Mg content in Al–Si–Mg alloys leads to the increase of volume fraction and size of the  $\pi$ -AlMgFeSi phase, which results in the low ductility.<sup>[20]</sup> Taylor *et al.*<sup>[21]</sup> pointed out that the solution treatment causes the transformation of  $\pi$ -AlMgFeSi phase to the small clustered  $\beta$ -AlFeSi phase when the Mg content is low (0.3 to 0.4 wt pct). Lu *et al.*<sup>[22]</sup> believed that the  $\pi$ -AlMgFeSi phase is usually limited only to the surface of  $\beta$ -AlFeSi phase since the following reaction is unlikely completed:



Yao and Taylor<sup>[23]</sup> performed solution treatment to Al–Si–Mg alloys and claimed that the fine needle-like particles formed are the  $\beta$ -AlFeSi phase plates similar to those in as-cast Al alloys but of much finer sizes. These  $\beta$ -AlFeSi phase plates are probably formed in the local regions where the Fe content becomes high by precipitation in the vicinity of the dissolving  $\pi$ -AlMgFeSi phase particles. It is known that Fe contents should be kept as low as practical, and a critical Fe content for an alloy was proposed<sup>[3]</sup>:

$$\text{wt pctFe} \approx 0.075 \times [\text{wt pctSi}] - 0.05 \quad [2]$$

According to Eq. [2], the critical Fe concentration is 0.4 to 0.5 wt pct in A356 alloy. Most of the previous studies<sup>[22,24,25]</sup> were performed with high Fe content (> 0.5 wt pct) and Mn in addition to modify the Fe-rich intermetallic compounds in Al alloy. However, there is a

limit of Fe content of about 0.2 wt pct in A356 alloy from ASM handbook,<sup>[26]</sup> which is far less than the critical Fe content. Investigation on Fe-rich intermetallic compounds in Al–Si–Mg alloy with low Fe content (< 0.4 wt pct) is less, and the microstructure evolution of Fe-rich intermetallic compounds in Al–Si–Mg cast alloys with low Fe content, especially the transformation between Fe-rich intermetallic compounds, is seldom discussed.

In this article, the Fe-rich intermetallic compounds in Al–Si–Mg cast alloy with the Fe content from 0.1 to 0.3 wt pct were investigated systematically. The microstructural morphology and the crystallographic orientation relationship were observed and analyzed, and the quantitative metallography analysis was conducted. The effect of the microstructure evolution of Fe-rich intermetallic compounds on mechanical properties was studied. The phase and morphology transformations of Fe-rich intermetallic compounds were summarized.

## II. EXPERIMENTAL PROCEDURES

The industrial A356 alloy and Al–10 wt pctFe master alloy were melted with different proportions in an electrical resistance furnace at 1023 K  $\pm$  5 K (750 °C  $\pm$  5 °C) to obtain Al–Si–Mg–Fe alloys with different Fe contents. Argon was piped into the melt for 5 min to remove the air. In addition, the melt was refined and modified at 993 K  $\pm$  5 K (720 °C  $\pm$  5 °C) by adding Al–5Ti–1B and Al–10Sr alloys, respectively. The temperature of melt was kept at 923 K to 953 K (650 °C to 680 °C), and then the melt was poured into the permanent mold, which was pre-heated at 523 K (250 °C). The measured chemical compositions of the casting alloys are shown in Table I. The metallographic samples were cut from the casting alloys by electrical discharge machining, polished by normal metallographic techniques and etched by the Keller solution (95 mL H<sub>2</sub>O, 2.5 mL HNO<sub>3</sub>, 1.5 mL HCl, and 1 mL HF) for 15 seconds.

The microstructure characteristics of the alloys were analyzed by optical microscopy (OM), scanning electron microscope (SEM, TESCANVEGA II), and energy-dispersive spectroscopy (EDS). X-ray diffraction (XRD, D/max 2500PC) was used to identify the phases in the samples. Twenty micrographs (each 82,737  $\mu\text{m}^2$ ) of each alloy were obtained by SEM-BSE in different areas, and quantitative metallography measurements were performed and analyzed by using Image pro-Plus6.0 software to provide statistical information of Fe-rich intermetallic compounds. The crystallographic orientation relationships of iron-rich intermetallic compounds were investigated with a transmission electron microscopy (TEM, FEI Tecnai G2 F20) before prepared by twin-jet polishing in a Struers TenuPol-5 machine. The electrolyte consisted of 30 vol pct HNO<sub>3</sub> in methanol and was kept at the temperature range from 238 K to 248 K (– 35 °C to – 25 °C).

The tensile tests were carried out by using the CMT-5305 universal testing machine at a crosshead speed of 1 mm/min. Tensile samples with a cross section of  $4 \times 2.5$  mm and gage length of 13 mm were cut from the alloys. In each group, five tensile samples were tested, and the average values of tensile strength, yield strength, and elongation were calculated. The fracture morphologies of the tensile samples were also observed by SEM for the analysis of the fracture mechanisms.

**Table I. Chemical Compositions of the Alloys in this Paper (Weight Percent)**

Alloy	Si	Mg	Fe	Ti	Al
0.1 Wt PctFe	6.6	0.32	0.09	0.12	bal.
0.2 Wt PctFe	6.62	0.3	0.21	0.14	bal.
0.3 Wt PctFe	6.57	0.31	0.33	0.14	bal.

### III. RESULTS

#### A. Microstructure of Fe-Rich Intermetallic Compounds

The typical microstructures of Al-7Si-0.3Mg alloys with different Fe contents were observed as shown in Figure 1. The Fe-rich intermetallic compounds can be distinguished in back-scattered electron (BSE) mode of SEM, and the Fe-rich intermetallic compounds of the gray script-like  $\pi$ -AlSiMgFe phase and bright needle-like  $\beta$ -AlFeSi phase can be observed. Meanwhile, the dark  $\alpha$ -Al phase and the gray Si phase can be seen in the background. When the Fe content is 0.1 wt pct as shown in Figure 1(a), the  $\pi$ -AlSiMgFe phase can be easily observed, and some  $\beta$ -AlFeSi phase existed in the alloy. In addition, almost all the intermetallic compounds distribute at the interdendritic region. However, the  $\pi$ -AlSiMgFe phase can be hardly observed when the Fe content is 0.2 wt pct. In 0.2 wt pctFe alloy, most of the Fe-rich intermetallic compounds are  $\beta$ -AlFeSi phase. In 0.3 wt pctFe alloy, there is plenty of  $\beta$ -AlFeSi phase formed. Besides, it should be noted that the  $\pi$ -AlSiMgFe phase is often observed to be closely connected to the

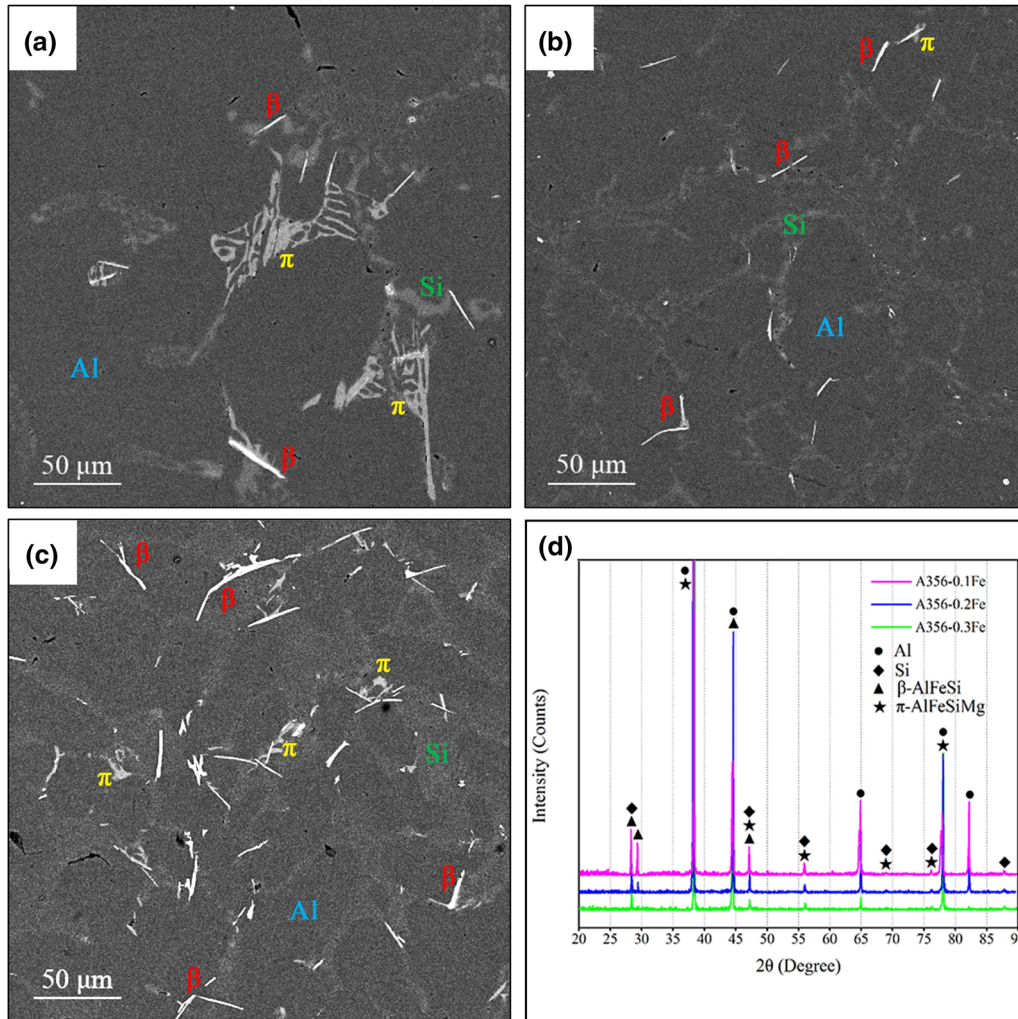


Fig. 1—Typical microstructures of Al-7Si-0.3Mg alloys with different Fe contents (a) 0.1 wt pctFe, (b) 0.2 wt pctFe, (c) 0.3 wt pctFe, and (d) XRD pattern of the alloys.



$\beta$ -AlFeSi phase. The XRD analysis results of samples are shown in Figure 1(d). When the Fe content is 0.1 wt pct, the  $\pi$ -AlSiMgFe phase tends to form. With the increase of Fe content, the formation of  $\beta$ -AlFeSi is promoted.

The morphologies of Fe-rich intermetallic compounds and the results of EDS mapping analysis in different alloys are shown in Figure 2. The EDS results clearly show the element distributions of Al, Si, Fe, and Mg, which confirms the Fe-rich intermetallic compounds. In 0.1 wt pctFe alloy, the major Fe-rich intermetallic compound is  $\pi$ -AlMgFeSi phase, and the morphology is script-like (shown in Figure 2(a)). In 0.2 wt pctFe alloy, as shown in Figure 2(b), the  $\beta$ -AlFeSi phase is formed with a needle-like morphology near the eutectic Si. Compared with Fe-rich intermetallic compounds in former alloys, Figure 2(c) shows that the  $\pi$ -AlMgFeSi phase with a script-like morphology is formed on the surface of the  $\beta$ -AlFeSi phase, which has a coarser needle-like morphology in 0.3 wt pctFe alloy. The 2D metallographic morphologies of Fe-rich intermetallic compounds show good agreement with the studies of Taylor *et al.*<sup>[3,4]</sup>

Figure 3 shows the deep etched 3D morphologies of Fe-rich intermetallic compounds in different alloys. The 3D morphology of  $\pi$ -AlMgFeSi phase in 0.1 wt pctFe alloy is shown in Figure 3(a). Compared with the morphology traditionally described in 2D cross-sectional view, the  $\pi$ -AlMgFeSi phase shows a morphology resembling seaweed after deep etching. Besides, a clearly layered structure can be observed on the 3D morphology of  $\pi$ -AlMgFeSi phase. The EDS result of point 1 indicates that the possible phases should be  $\pi$ -Al<sub>8</sub>Mg<sub>3</sub>FeSi<sub>6</sub> phase and Si phase. The dominant Fe-rich intermetallic compound in 0.2 wt pctFe alloy is  $\beta$ -AlFeSi phase, and Figure 3(b) shows the 3D morphology. An irregular polygonal platelet-like morphology can be observed, which is similar to the studies.<sup>[27,28]</sup> The EDS result of point 2 confirms the existence of element Al, Si, and Fe. In 0.3 wt pctFe alloy, the 3D morphology of the  $\pi$ -AlMgFeSi phase forming on the  $\beta$ -AlFeSi phase is shown in Figure 3(c). Compared with the morphology of  $\beta$ -AlFeSi phase in 0.2 wt pctFe alloy, the platelets of  $\beta$ -AlFeSi phase become coarser and thicker in 0.3 wt pctFe alloy, and the  $\pi$ -AlMgFeSi phase is directly formed on the surface of the coarser platelet-like  $\beta$ -AlFeSi phase. The EDS results of point 3 and point 4 show that the  $\pi$ -AlMgFeSi phase is combined with the  $\beta$ -AlFeSi phase. There is also a layered structure on the 3D morphology of  $\pi$ -AlMgFeSi, formed on the  $\beta$ -AlFeSi phase. However, compared with  $\pi$ -AlMgFeSi in 0.1 wt pctFe alloy, the layered structure of  $\pi$ -AlMgFeSi phase formed on the surface of the coarser platelets-like  $\beta$ -AlFeSi in 0.3 wt pctFe alloy is not as regular as in 0.1 wt pctFe alloy.

The TEM images of the Fe-rich intermetallic compounds in 0.1 and 0.2 wt pctFe alloys are shown in Figure 4. The selected area electron diffraction (SAED) patterns and EDS spectra indicate that the Fe-rich intermetallic compounds in 0.1 and 0.2 wt pctFe alloys were the hexagonal  $\pi$ -AlMgFeSi phase and the

monoclinic  $\beta$ -AlFeSi phase, respectively. The results agree well with the  $\pi$ -AlMgFeSi phase and the  $\beta$ -AlFeSi phase observed by Becker *et al.*<sup>[29]</sup>

Figure 5 shows the results of TEM analysis of the Fe-rich intermetallic compound in 0.3 wt pctFe alloy. The bright-field image of nucleation and growth of  $\pi$ -AlMgFeSi phase on massive platelet  $\beta$ -AlFeSi phase is shown in Figure 5(a). The EDS analysis result and the SAED pattern of  $\beta$ -AlFeSi phase and  $\pi$ -AlMgFeSi phase are shown in Figures 5(b), (d) and (c), (e), respectively. Figure 5(f) shows the HRTEM image and the relative FFT analysis SAED pattern of the interface area between  $\beta$ -AlFeSi phase and  $\pi$ -AlMgFeSi phase. The interface between  $\beta$ -AlFeSi phase and  $\pi$ -AlMgFeSi phase is smooth, and it is noted that there is a transition region, which is 0.4 nm, at the interface. The FFT analysis SAED pattern of the interface indicated that the transition region is amorphous. Compared with the SAED patterns of  $\beta$ -AlFeSi phase and  $\pi$ -AlMgFeSi phase (Figures 5(h) and (i)), the crystallographic orientation relationship between  $\beta$ -AlFeSi phase and  $\pi$ -AlMgFeSi phase can be proposed as  $(\bar{1}10)_{\beta} \parallel (1\bar{2}10)_{\pi}$ .

## B. Statistical Analysis of Fe-Rich Intermetallic Compounds

The quantitative results of Fe-rich intermetallic compounds of the  $\beta$ -AlFeSi phase and the  $\pi$ -AlMgFeSi phase were analyzed statistically in this part. Figure 6(a) shows the number and volume fraction of the  $\beta$ -AlFeSi phase in different Fe content alloys. Both are extremely influenced by Fe content. The whole measured field is around  $1.65 \times 10^6 \mu\text{m}^2$ . With the increase of Fe content, both the number and volume fraction of the  $\beta$ -AlFeSi phase increase. In 0.1 wt pctFe alloy, the number and volume fraction of  $\beta$ -AlFeSi phase is 508 and 0.4 pct, respectively. There is little  $\beta$ -AlFeSi phase, and the size is small. When Fe content is increased to 0.2 wt pct, the amount and the volume fraction of  $\beta$ -AlFeSi phase increase significantly. The number of  $\beta$ -AlFeSi phase is increased to 1181, and the volume fraction is increased to 0.6 pct. Besides, the average size of  $\beta$ -AlFeSi phase is about  $8.65 \mu\text{m}^2$ . When the Fe content is increased to 0.3 wt pct, the number of  $\beta$ -AlFeSi phase increases to 1323. The volume fraction has a significant increase, and the volume fraction sharply increases to 1.1 pct. The average size of  $\beta$ -AlFeSi phase increases to  $14.06 \mu\text{m}^2$ . The increments of the number and the volume fraction are approximately 132.5 and 50.0 pct when the Fe content increases from 0.1 to 0.2 wt pct. In addition, the increments of the number and the volume fraction change to 12.0 and 83.3 pct when the Fe content further increases from 0.2 to 0.3 wt pct. This indicates that the nucleation of  $\beta$ -AlFeSi phase is much easier than the growth in 0.2 wt pctFe alloy. When the Fe content further increases, the  $\beta$ -AlFeSi can not only nucleate but also sufficiently grow in 0.3 wt pctFe alloy.

Figure 6(b) shows the number and volume fraction of the  $\pi$ -AlMgFeSi phase in different Fe content alloys. With the increase of Fe content, the number and volume fraction of the  $\pi$ -AlMgFeSi phase decrease at first and

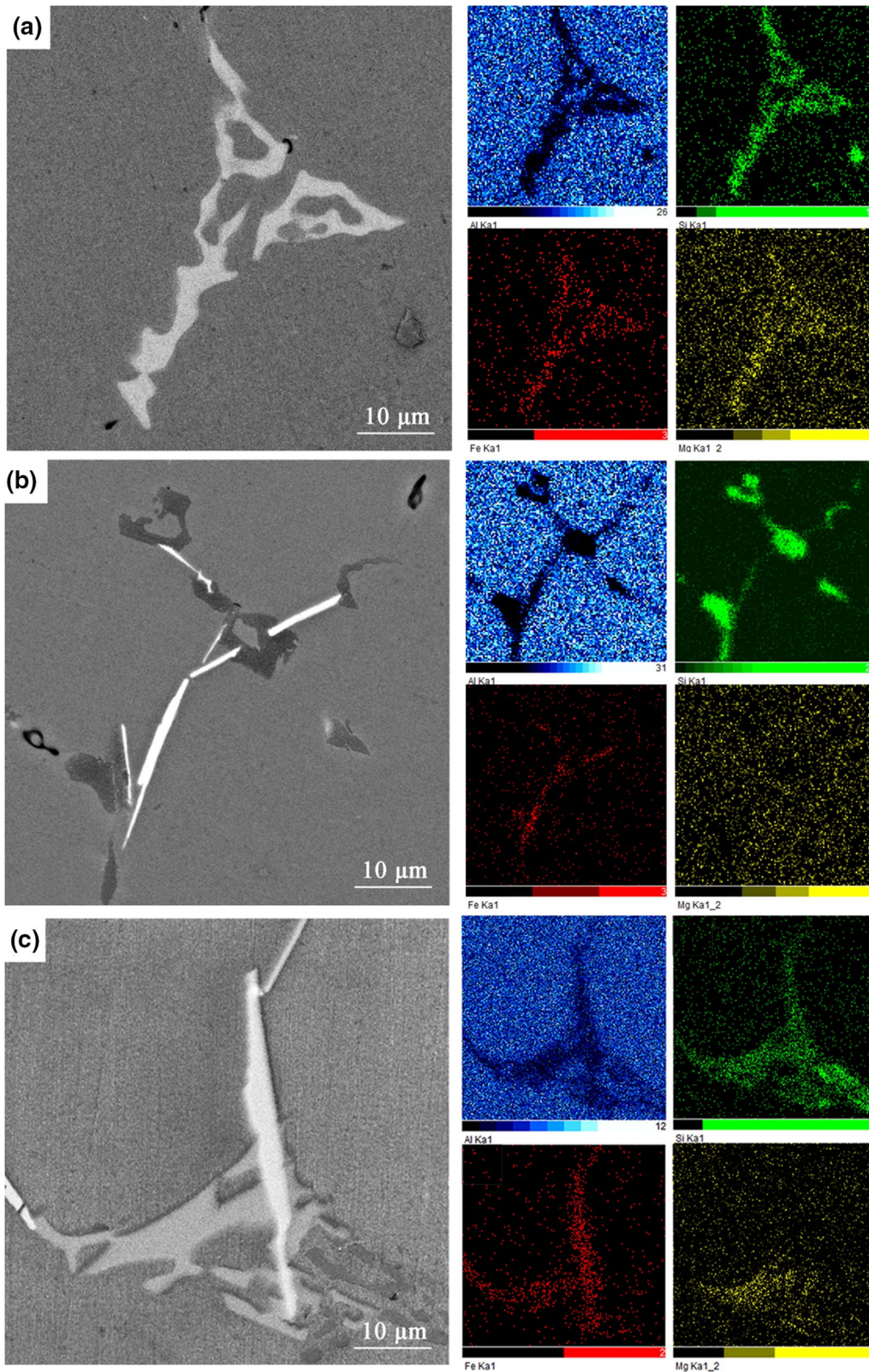


Fig. 2—Morphologies of Fe-rich intermetallic compounds and the corresponding EDS results of different alloys: (a) 0.1 wt pctFe, (b) 0.2 wt pctFe, and (c) 0.3 wt pctFe.

then increase. When the amount of Fe is 0.1 wt pct, the number and volume fraction of  $\pi$ -AlMgFeSi phase are

1675 and 1.4 pct, respectively. The average size of the  $\pi$ -AlMgFeSi phase is  $14.04 \mu\text{m}^2$ . In 0.2 wt pctFe alloy,



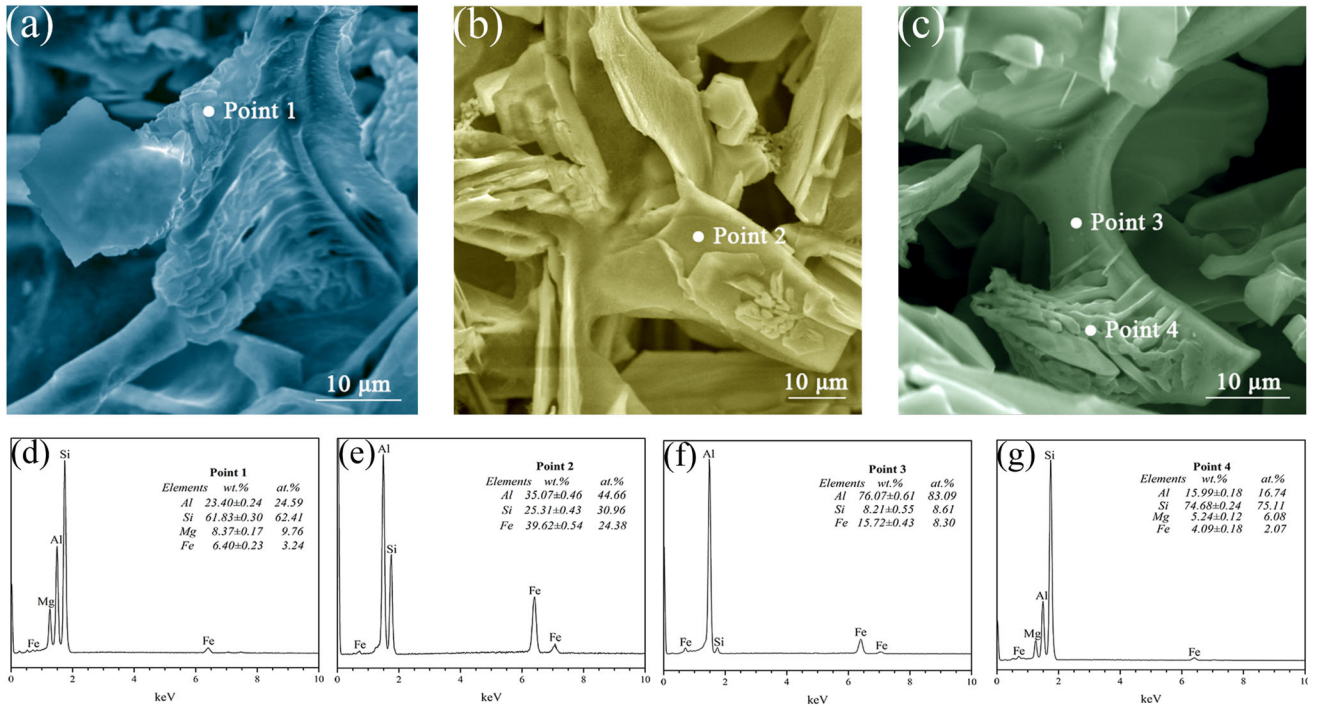


Fig. 3—Three-dimensional morphologies of Fe-rich intermetallic compounds in (a) 0.1 wt pctFe, (b) 0.2 wt pctFe, (c) 0.3 wt pctFe alloy, and (d) through (g) the corresponding EDS results in (a) through (c).

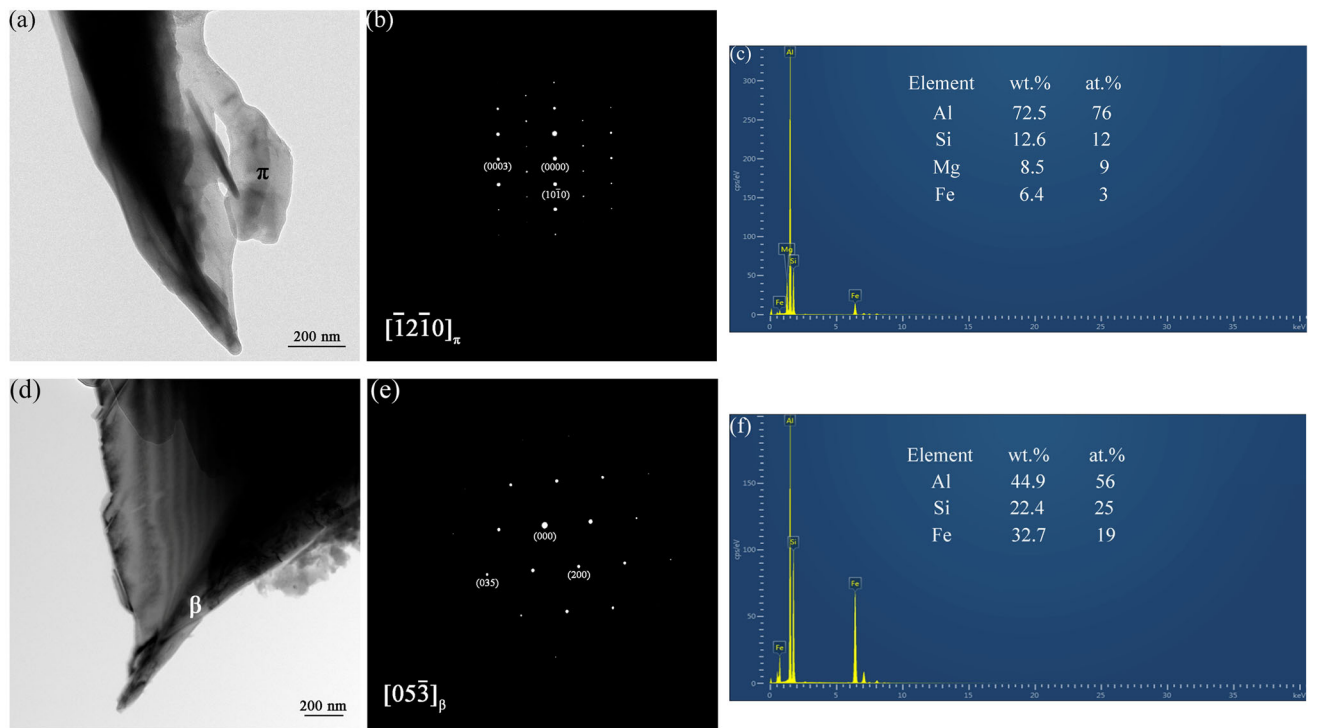


Fig. 4—(a) TEM bright-field image of  $\pi$ -AlMgFeSi phase in 0.1 wt pctFe alloy, (b) the SAED pattern of  $\pi$ -AlMgFeSi phase in (a), (c) the corresponding EDS results of  $\pi$ -AlMgFeSi phase in (a), (d) TEM bright-field image of  $\beta$ -AlFeSi phase in 0.2 wt pctFe alloy, (e) the SAED pattern of  $\beta$ -AlFeSi phase in (d), and (f) the corresponding EDS results of  $\beta$ -AlFeSi phase in (d).

the number of  $\pi$ -AlMgFeSi phase decreases to 990, and the volume fraction decreases to 0.3 pct. The average size of  $\pi$ -AlMgFeSi phase is reduced to  $4.68 \mu\text{m}^2$ . This

means that the formation of  $\pi$ -AlMgFeSi phase is restrained in 0.2 wt pctFe alloy. In 0.3 wt pctFe alloy, both the number and the volume fraction of the

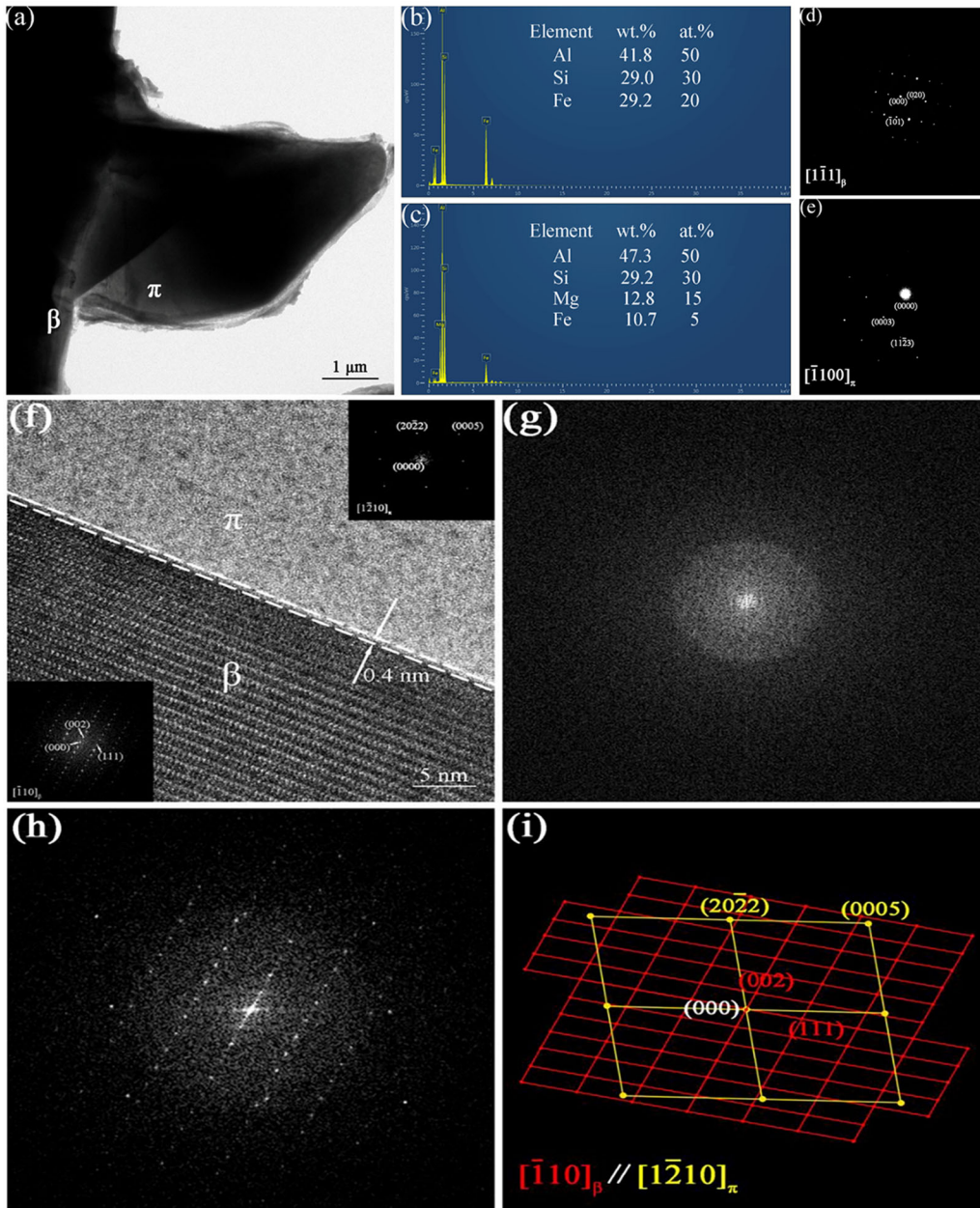


Fig. 5—(a) TEM bright-field image of  $\pi$ -AlMgFeSi phase on  $\beta$ -AlFeSi phase in 0.3 wt pctFe alloy, (b) and (c) the corresponding EDS results of  $\beta$ -AlFeSi phase and  $\pi$ -AlMgFeSi phase in (a), (d) and (e) the SAED pattern of  $\beta$ -AlFeSi phase and  $\pi$ -AlMgFeSi phase from a same electron beam direction in (a). (f) The HRTEM image and the relative FFT analysis SAED pattern of the interface area between  $\beta$ -AlFeSi phase and  $\pi$ -AlMgFeSi phase. (g) The FFT analysis SAED pattern of the interface. (h) and (i) The SAED pattern relationship between  $\beta$ -AlFeSi phase and  $\pi$ -AlMgFeSi phase in the interface area.

$\pi$ -AlMgFeSi phase have a noticeable increase compared with that in 0.2 wt pctFe alloy. The amount and volume fraction of  $\pi$ -AlMgFeSi phase in 0.3 wt pctFe alloy increase to 2641 and 1.0 pct, respectively. The average size of  $\pi$ -AlMgFeSi phase is about  $6.35 \mu\text{m}^2$ . This indicates that the formation of  $\pi$ -AlMgFeSi phase is promoted in 0.3 wt pctFe alloy. This phenomenon is in agreement with the previous research by Liu *et al.*<sup>[30]</sup>

To investigate the influence of various Fe contents on the growth of the  $\beta$ -AlFeSi phase, approximately 100 of the  $\beta$ -AlFeSi phase in the alloys with different Fe contents were randomly chosen and the aspect ratio

(length to thickness ratio) was measured. Figure 7 shows the distribution of the aspect ratio of the  $\beta$ -AlFeSi phase in different alloys, which obviously shows Gaussian distribution. When the Fe content is 0.1 wt pct, the aspect ratio is mainly  $< 10$ , and the ratio mainly ranges from 2 to 6. In the fitting curve, the peak corresponding to aspect ratio is 4.3. In 0.2 wt pctFe alloy, the aspect ratio almost set in 10 to 20. When the aspect ratio is 12.9, the fitting curve reaches the peak value. With the further increase of Fe content, the distribution range of the aspect ratio is much wider, and the main aspect ratio ranges from 20 to 30. The aspect ratio peak value is 24.0.

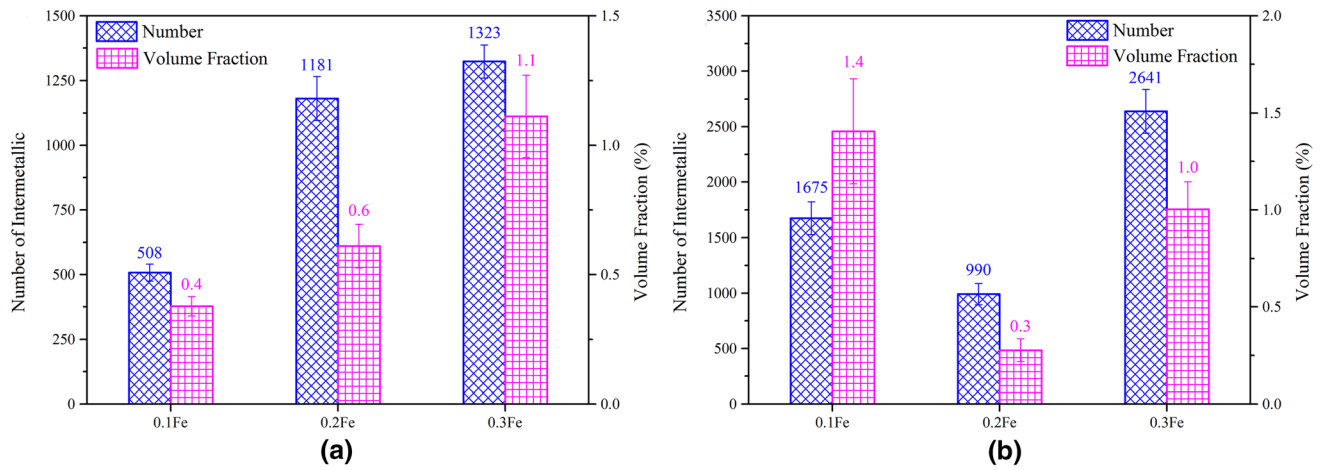


Fig. 6—Number and volume fraction of Fe-rich intermetallic compounds in the alloys with different Fe contents: (a)  $\beta$ -AlFeSi phase and (b)  $\pi$ -AlMgFeSi phase.

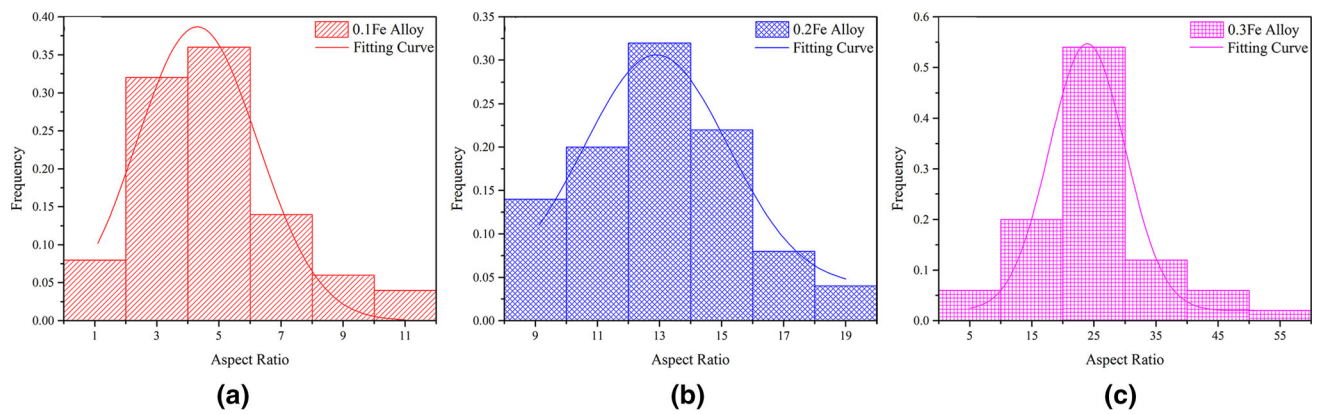


Fig. 7—The aspect ratio distribution of  $\beta$ -AlFeSi phase with varying Fe contents: (a) 0.1 wt pctFe alloy, (b) 0.2 wt pctFe alloy, (c) 0.3 wt pctFe alloy.

The results indicate that the aspect ratio of  $\beta$ -AlFeSi phase is promoted with the increase of the Fe content because with the increase of Fe content, more Fe atoms distribute in the residual melt, and  $\beta$ -AlFeSi phase can grow more easily during solidification. It also can be seen that the morphology of  $\beta$ -AlFeSi phase becomes slender and sharper as Fe content increases.

### C. Tensile Properties of Al–Si–Mg Alloys with Different Fe Contents

Tensile tests were performed to investigate the effect of Fe-rich intermetallic compounds on the mechanical properties of Al–Si–Mg alloys. Figure 8 shows the tensile properties of Al–Si–Mg alloys with different Fe contents. The results indicate that the tensile properties reduce at first and then increase with the increase of Fe content from 0.1 to 0.3 wt pct. In 0.1 wt pctFe alloy, the elongation is about 7.7 pct, and the ultimate tensile strength and yield strength are about 186 MPa and 80 MPa, respectively. When the Fe content is increased to 0.2 wt pct, the elongation decreases to 5.4 pct, and the ultimate tensile strength and yield strength are about

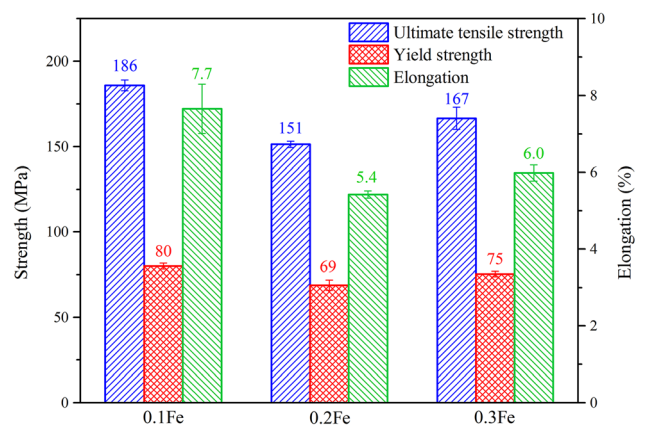


Fig. 8—The values of ultimate tensile strength, 0.2 pct proof yield strength, and elongation of the Al–7Si–0.3Mg– $x$ Fe alloy.

151 and 69 MPa, respectively. Compared with 0.1 wt pctFe alloy, the tensile properties of 0.2 wt pctFe alloy are reduced. The elongation is decreased by 9.4 pct, and the ultimate tensile strength and yield strength are



decreased by 5.2 and 8.6 pct, respectively. For 0.3 wt pctFe alloy, the tensile properties are increased massively. The elongation increases to 6.0 pct, and the ultimate tensile strength (UTS) and yield strength (YS) are improved to 167 and 75 MPa, respectively. Compared with the tensile properties of 0.2 wt pctFe alloy, the elongation is increased by 11.1 pct, and the ultimate tensile strength and the yield strength are increased by 10.6 and 8.7 pct, respectively.

To evaluate the tensile property, a quality index was calculated, considering both ultimate tensile strength and elongation of the alloys. The quality index ( $Q$ ) can be calculated by the following equation as<sup>[31]</sup>:

$$Q[\text{MPa}] = \text{UTS} + a \times \log(\text{elongation}) \quad [3]$$

where  $a$  is 150 for Al–Si–Mg alloys. It should be noted that the true tensile properties described by the combination of strength and ductility are much more objective than by either the tensile strength or the elongation alone.<sup>[32,33]</sup> The results indicate that the value of  $Q$  decreases from 319 to 261 MPa and then increases to 284 MPa with the increase of Fe content. Therefore, the as-cast alloy with 0.3 wt pctFe has a better mechanical property than that with 0.2 wt pctFe.

Figure 9 exhibits the SEM fractographs of the tensile samples of Al–7Si–0.3Mg alloys with different Fe contents under as-cast condition. As can be seen in Figure 9(a), the fracture surface of 0.1 wt pctFe tensile sample shows a mixed quasi-cleavage and dimple morphology, which is in agreement with the previous study.<sup>[34]</sup> Figures 9(b) and (c) shows the Fe-rich intermetallic compound on the fracture surface of 0.1 wt pctFe tensile sample. The amount and size of  $\beta$ -AlFeSi phase are extremely small. However, it still might be the crack initiator. With the addition of 0.2 wt pct Fe as shown in Figure 9(d), the flat areas can be observed clearly on the fracture surface. The quantity of dimple existed around the flat areas decreases. The tearing ridge, as a typical brittle fracture feature, can also be seen in Figure 9(d). According to the results of EDS point analysis, the microstructure in flat areas is  $\beta$ -AlFeSi phase (Figure 9(e)). Compared with  $\beta$ -AlFeSi phase in 0.1 wt pctFe alloy, the size of  $\beta$ -AlFeSi in 0.2 wt pctFe alloy increases, resulting in the decrease of tensile strength. With the further increase of Fe content to 3 wt pct, the size of  $\beta$ -AlFeSi phase further increases, and several large flat areas can be observed on the fracture surfaces in Figure 9(f). The dimple appears again around flat areas. Besides, the dimple size becomes smaller compared with Figure 9(b), which leads to the improvement of the tensile properties. In the region of dimple, the elements Fe and Mg are enriched at point 5 (Figure 9(g) and EDS results in Figure 9(h)), which can be identified as  $\pi$ -AlMgFeSi phase. In 0.3 wt pctFe tensile sample, the  $\pi$ -AlMgFeSi phase on  $\beta$ -AlFeSi phase can not only reduce the negative effect of  $\beta$ -AlFeSi phase on tensile strength, but can also induce the formation of smaller dimples to improve the elongation of the alloy.

Figure 10 shows the cross-section images of the fracture profile of Al–7Si–0.3Mg alloy samples with different Fe contents and that the fracture mainly extends along the grain boundary. Therefore, the Fe content in the alloy has a direct influence on the initiation and propagation of cracks. There are many eutectic Si phase and Fe-rich phases distributed around the fracture. Similar results were obtained by Çadırılı *et al.*<sup>[35]</sup> Higher magnification results (Figure 10(b)) show that in 0.1 wt pctFe alloy, there are many micro-cracks in the  $\pi$ -AlMgFeSi phase besides the microcracks in the eutectic Si structure. The directions of the cracks are perpendicular to the tensile stress direction. The small cracks of Fe-rich phase in the figure are marked by white arrows. In 0.2 wt pctFe alloy, the crack propagates along the surface of the  $\beta$ -AlFeSi phase, and there are almost no microcracks in/across the  $\beta$ -AlFeSi phase as shown in Figures 10(c) and (d). In 0.3 wt pctFe alloy, the microcracks not only initiate and propagate in  $\pi$ -AlMgFeSi phase, but also propagate across to the  $\beta$ -AlFeSi phase, resulting in the break of the needle-like  $\beta$ -AlFeSi phase as shown in Figures 10(e) and (f).

#### IV. DISCUSSION

The Scheil module of Thermo-Calc software combined with TCS Al-based alloy database<sup>[36]</sup> was used to predict the phases formed during the solidification of A356 alloys with various Fe contents. The curves of temperature as a function of solid fraction are shown in Figure 11. It shows that the identity of Fe-rich intermetallic compounds as well as phase transformation temperature changes with the increase of Fe content. Thermo-Calc predictions show that the reactions are the same when the Fe content is  $< 0.4$  wt pct. The reactions of solidification sequence in A356 alloy are presented in Table II.<sup>[6]</sup> The Fe-rich intermetallic compounds start to form just after the end of Si eutectic reaction. The ternary eutectic reaction (Reaction 4 in Table II, the blue line in Figure 11) is sensitized to Fe content and becomes the main reaction as Fe content increases. For A356-0.1 wt pctFe alloy, Thermo-Calc prediction shows that the temperature range of ternary eutectic reaction is 842 K to 834 K (569 °C to 561 °C). Increasing the Fe content enlarges the temperature range for ternary eutectic reaction. In addition, with the increase of Fe content, the start temperature of the reaction for  $\beta$ -AlFeSi phase is higher, and the eutectic Si reaction is restrained. The proportion of  $\beta$ -AlFeSi phase in all the Fe-rich phases increases, and thus  $\beta$ -AlFeSi phase gradually becomes the dominant phase with the increase of Fe content.

According to Al–Si–Fe–Mg quaternary diagram, the  $\pi$ -AlMgFeSi phase is formed on the surface of  $\beta$ -AlFeSi phase in 0.3 wt pctFe alloy because of the eutectic reaction. However, the morphology of  $\pi$ -AlMgFeSi phase formed on the  $\beta$ -AlFeSi phase is different from the sandwich-like morphology mentioned in previous

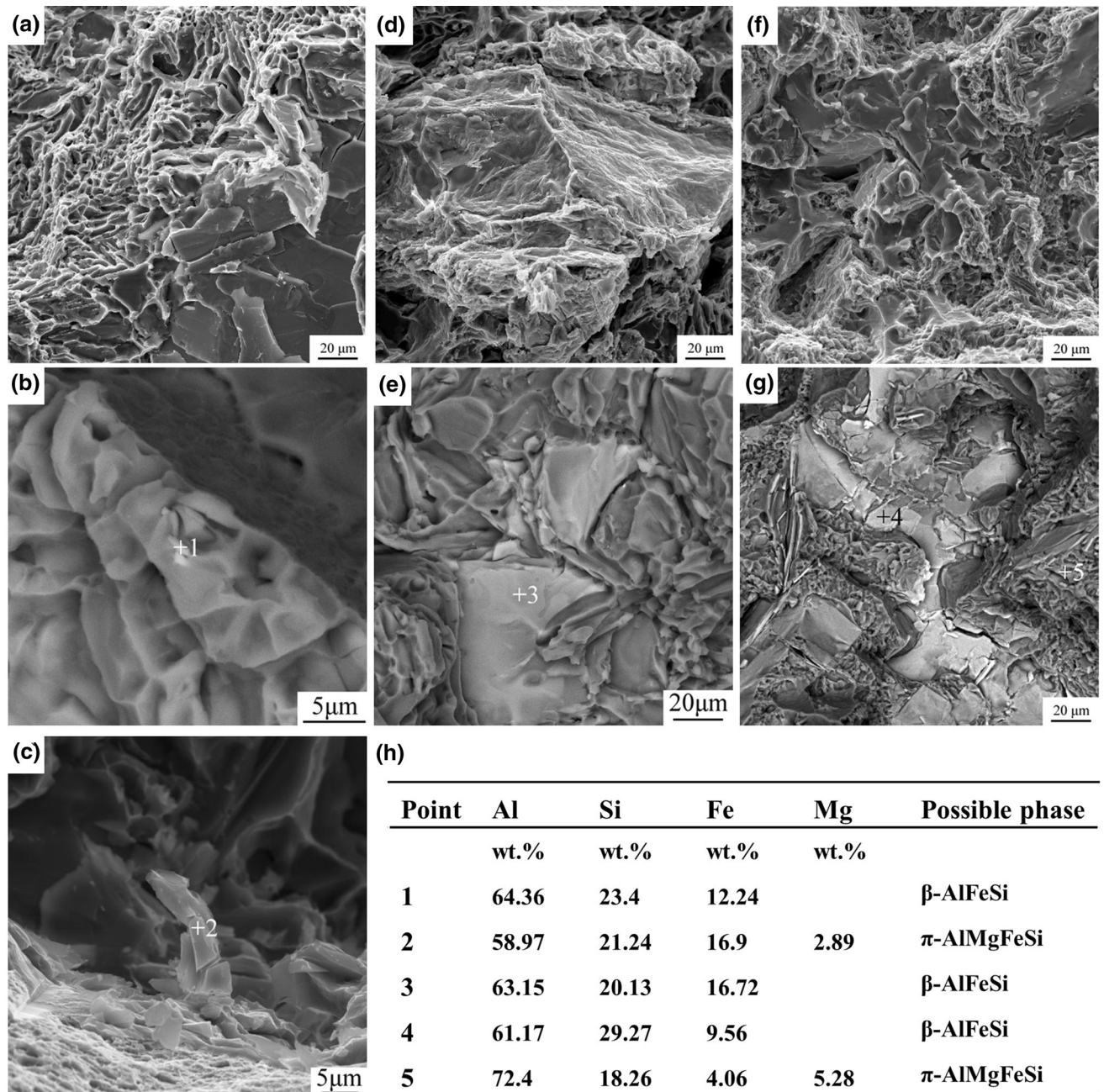


Fig. 9—SEM fractographs of Al-7Si-0.3Mg alloy samples with different Fe contents: (a) 0.1 wt pct Fe, (b) and (c) higher magnification of (a), (d) 0.2 wt pct Fe, (e) higher magnification of (d), (f) 0.3 wt pct Fe, (g) higher magnification of (f), and (h) the corresponding EDS results.

research.<sup>[4]</sup> The morphology of  $\pi$ -AlMgFeSi phase growing from  $\beta$ -AlFeSi phase is more similar to a script-like morphology. Lu *et al.*<sup>[22]</sup> reported that the quaternary eutectic reaction was not completed, and thus the morphology of  $\pi$ -AlMgFeSi phase growing from  $\beta$ -AlFeSi phase was not a sandwich-like morphology. In this study, the sufficient growth of  $\beta$ -AlFeSi phase in 0.3 wt pctFe alloy could facilitate the formation of  $\pi$ -AlMgFeSi phase. The formation model of  $\pi$ -AlMgFeSi phase growing from  $\beta$ -AlFeSi phase is shown in Figure 12. During the solidification process, the element Mg is enriched around  $\beta$ -AlFeSi phase. In 0.2 wt pctFe

alloy, the growth of  $\beta$ -AlFeSi phase is not ample, and Mg concentration in the adjacent melt is not enough for the formation of the  $\pi$ -AlMgFeSi phase. Besides, the  $\beta$ -AlFeSi phase tends to form with the increase of Fe content, resulting in the decrease of  $\pi$ -AlMgFeSi phase in 0.2 wt pctFe alloy. In 0.3 wt pctFe alloy, the  $\beta$ -AlFeSi phase grows adequately, and plenty of  $\beta$ -AlFeSi phase is formed in the alloy. The coarser platelet  $\beta$ -AlFeSi phase likely grows to interconnect and results in the enrichment of Mg element in the local areas. Therefore, the  $\pi$ -AlMgFeSi phase is formed within the high Mg concentration region.



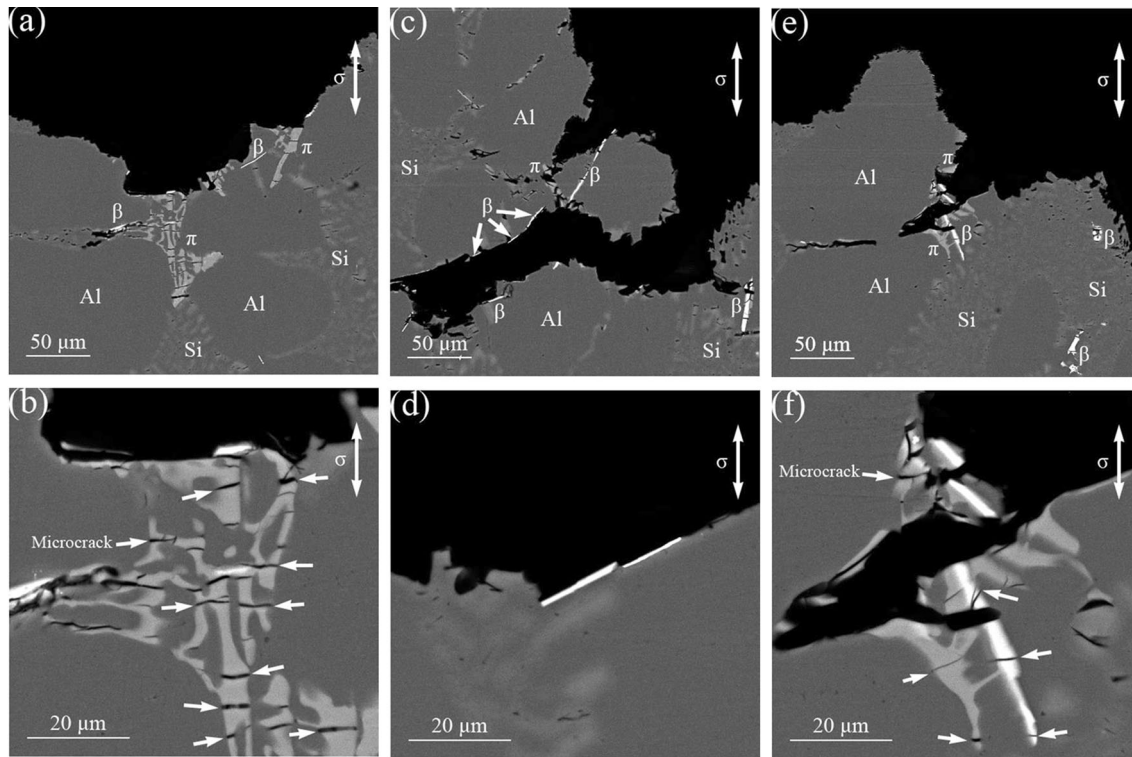


Fig. 10—The cross-section SEM images of fracture profile of Al-7Si-0.3Mg alloy samples with different Fe contents: (a) and (b) 0.1 wt pct Fe, (c) and (d) 0.2 wt pct Fe, (e) and (f) 0.3 wt pct Fe.

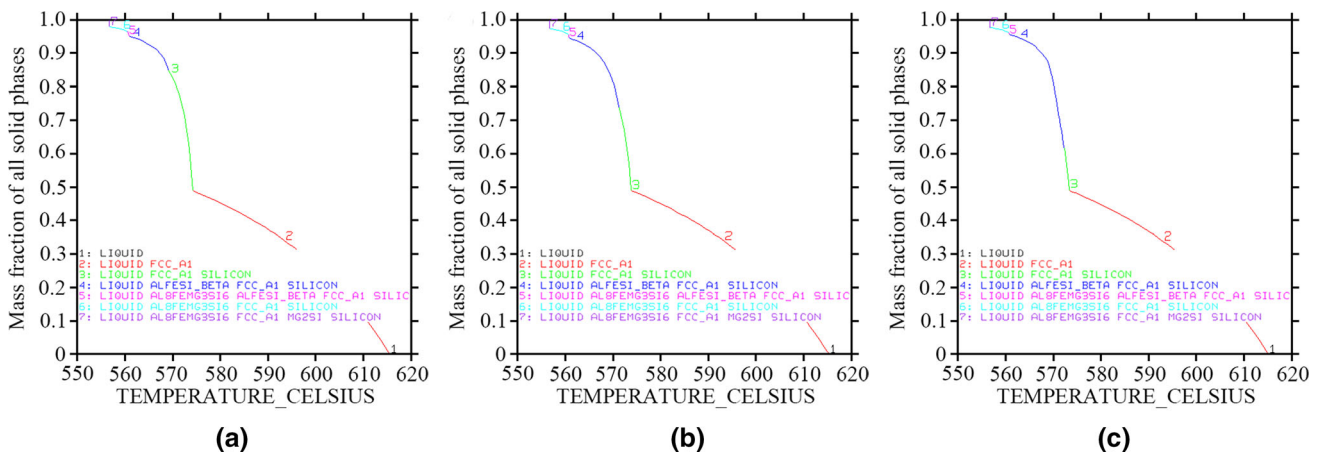


Fig. 11—Temperature as a function of solid fraction predicted by Thermo-Calc: (a) 0.1 wt pct Fe, (b) 0.2 wt pct Fe, and (c) 0.3 wt pct Fe.

Table II. Solidification Reactions Observed in A356 Alloy<sup>61</sup>

No.	Possible Reaction	Temperature [K(°C)]
1	$L \rightarrow \alpha - \text{Al}$	884 to 888 (611 to 615)
2	$L \rightarrow \alpha - \text{Al} + \text{Si}$	850 (577)
3	$L \rightarrow \alpha - \text{Al} + \text{Si} + \beta - \text{Al}_5\text{FeSi}$	848 (575)
4	$L + \beta - \text{Al}_5\text{FeSi} \rightarrow \alpha - \text{Al} + \text{Si} + \pi - \text{Al}_8\text{Mg}_3\text{FeSi}_6$	840 (567)
5	$L \rightarrow \alpha - \text{Al} + \text{Si} + \text{Mg}_2\text{Si} + \pi - \text{Al}_8\text{Mg}_3\text{FeSi}_6$	827 (554)

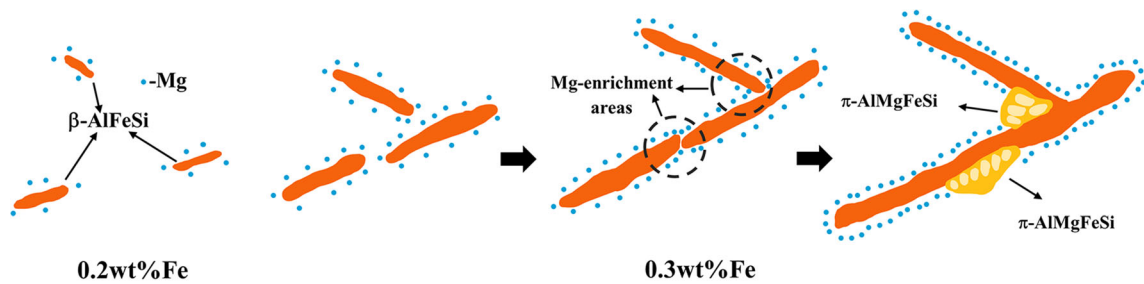


Fig. 12—Schematic illustration of the formation model of  $\pi$ -AlMgFeSi phase growing from  $\beta$ -AlFeSi phase.

In 0.1 wt pctFe alloy, the Fe-rich intermetallic compound is almost  $\pi$ -AlMgFeSi phase. The layered structure may increase the adhesive strength between the  $\pi$ -AlMgFeSi phase and the matrix. With the increase of Fe content, the tensile properties of 0.2 wt pctFe alloy are reduced. The growth of  $\pi$ -AlMgFeSi phase is restrained, while the nucleation of  $\beta$ -AlFeSi phase is promoted. However, the microstructure of  $\beta$ -AlFeSi phase is harmful to the tensile properties. The volume fraction of  $\beta$ -AlFeSi phase increases, which indicates that the size of  $\beta$ -AlFeSi phase in 0.2 wt pctFe alloy is larger than that of 0.1 wt pctFe alloy. This means that the  $\beta$ -AlFeSi phase with shaper needle-like structure promoted in 0.2 wt pctFe alloy is detrimental to mechanical properties. Although the morphology of  $\beta$ -AlFeSi phase is slender and sharper with Fe content and continues increasing, the  $\pi$ -AlMgFeSi phase can grow on the coarser platelet  $\beta$ -AlFeSi phase, and the growth direction of  $\pi$ -AlMgFeSi phase is different from that of needle-like  $\beta$ -AlFeSi phase. The layered structure of  $\pi$ -AlMgFeSi phase formed on the coarser platelet  $\beta$ -AlFeSi phase not only enhances the adhesive strength between the  $\beta$ -AlFeSi and the matrix, but also wraps on the  $\beta$ -AlFeSi surface to reduce the detrimental effect on mechanical properties of the  $\beta$ -AlFeSi phase. Therefore, the tensile properties of 0.3 wt pctFe alloy increase compared with those of 0.2 wt pctFe alloy.

## V. CONCLUSIONS

In this article, the effect of the Fe-rich intermetallic compounds on mechanical properties of Al-7Si-0.3Mg alloys with low iron content ( $< 0.4$  wt pct) was investigated, and the conclusions are as follows:

1. With the increase of Fe content, the dominant Fe-rich intermetallic compounds change from  $\pi$ -AlMgFeSi phase to  $\beta$ -AlFeSi phase, and then the  $\pi$ -AlMgFeSi phase can form on the  $\beta$ -AlFeSi phase. Meanwhile, the 2D morphologies of Fe-rich intermetallic compounds transform from the script-like to needle-like, and then the script-like phase appears on the surface of the needle-like phase. The 3D morphology of  $\pi$ -AlMgFeSi phase resembled seaweed, and a clearly layered structure is observed on the 3D morphology of  $\pi$ -AlMgFeSi phase. For the  $\beta$ -AlFeSi phase, the 3D morphology is irregular polygonal

platelet-like. In 0.3 wt pctFe alloy, the layered structure of  $\pi$ -AlMgFeSi phase, which forms on the surface of platelets-like  $\beta$ -AlFeSi phase, is not as regular as in 0.1 wt pctFe alloy.

2. In 0.3 wt pctFe alloy, the  $\pi$ -AlMgFeSi phase often grows on the surface of the  $\beta$ -AlFeSi phase, and the crystallographic orientation relationship is proposed as  $[1100]_{\pi} \parallel [111]_{\beta}$  and  $(1123)_{\pi} \parallel (202)_{\beta}$ . In 0.2 wt pctFe alloy, the nucleation of the  $\beta$ -AlFeSi phase is promoted compared with that in 0.1 wt pctFe alloy, while in 0.3 wt pctFe alloy the growth of the  $\beta$ -AlFeSi phase is boosted, which may lead to the formation of  $\pi$ -AlMgFeSi phase on the  $\beta$ -AlFeSi phase in 0.3 wt pctFe alloy due to the generation of the Mg enriched areas.
3. With the increase of Fe content, the  $\pi$ -AlMgFeSi phase, resembling a seaweed morphology, and a layered structure transform into the  $\beta$ -AlFeSi phase with an irregular polygonal platelet-like morphology, resulting in the decrease of tensile properties. With further increase of the Fe content, the layered structure of the  $\pi$ -AlMgFeSi phase formed on the surface of the platelet-like  $\beta$ -AlFeSi phase reduces the negative effect of  $\beta$ -AlFeSi phase on the mechanical properties. The microstructure morphology of  $\pi$ -AlMgFeSi phase on the  $\beta$ -AlFeSi phase enhances the adhesive strength between the  $\beta$ -AlFeSi phase and the matrix, which also induces the formation of smaller dimples improving the elongation of the alloys.

## ACKNOWLEDGMENTS

The authors acknowledge the financial support from the National Natural Science Foundation of China (No. 51875062).

## AUTHOR CONTRIBUTIONS

JZ: Conceptualization, Investigation, Supervision. YG: Investigation, Data curation, Writing—review & editing. BX: Writing—review and editing. CG: Investigation, Data curation, Writing—original draft. YW: Writing—review and editing. QT: Methodology, Formal analysis.



## DATA AVAILABILITY

All data that support the findings of this study are available from the corresponding author upon reasonable request.

## CONFLICT OF INTERESTS

The authors declare no competing interests.

## REFERENCES

1. A. Taub, E. De Moor, A. Luo, D.K. Matlock, J.G. Speer, and U. Vaidya: *Annu. Rev. Mater. Res.*, 2019, vol. 49, pp. 327–59.
2. K. Chanyathunyaroj, U. Patakham, S. Kou, and C. Limmaneevichitr: *J. Alloys Compd.*, 2017, vol. 692, pp. 865–75.
3. J.A. Taylor: *Procedia Mater. Sci.*, 2012, vol. 1, pp. 19–33.
4. L. Sweet, S.M. Zhu, S.X. Gao, J.A. Taylor, and M.A. Easton: *Metall. Mater. Trans. A*, 2011, vol. 42A, pp. 1737–49.
5. O. Elsebaie, A.M. Samuel, and F.H. Samuel: *J. Mater. Sci.*, 2011, vol. 46, pp. 3027–45.
6. A. Gorny, J. Manickaraj, Z. Cai, and S. Shankar: *J. Alloys Compd.*, 2013, vol. 577, pp. 103–24.
7. Z. Li and H. Yan: *J. Rare Earths*, 2015, vol. 33, pp. 995–1003.
8. S. Murali, K.S. Raman, and K.S.S. Murthy: *Mater. Charact.*, 1994, vol. 33, pp. 99–112.
9. C.J. Narducci, G.L. Brollo, R.H.M. de Siqueira, A.S. Antunes, and A.J. Abdalla: *Sci. Rep.*, 2021, vol. 11, pp. 1–14.
10. A.M. Samuel, Y. Zedan, H.W. Doty, V. Songmene, and F.H. Samuel: *Int. J. Met.*, 2021, <https://doi.org/10.1007/s40962-021-00613-8>.
11. M.H. Khan, A. Das, Z. Li, and H.R. Kotadia: *Intermetallics*, 2021, vol. 132, pp. 1–10.
12. R. Qin, R.F. Yan, Z.P. Guan, G.Q. Zhang, J.W. Song, M.W. Ren, and J.G. Wang: *Mater. Res. Express*, 2021, vol. 8, p. 026518. <https://doi.org/10.1088/2053-1591/abe5f0>.
13. L.A. Narayanan, F.H. Samuel, and J.E. Gruzleski: *Metall. Mater. Trans. A*, 1995, vol. 26A, pp. 2161–74.
14. T. Liu, M. Karkkainen, L. Nastac, V. Arvikar, I. Levin, and L.N. Brewer: *Intermetallics*, 2020, vol. 126, p. 106814.
15. R. Wagner, M. Seleznev, H. Fischer, R. Ditscherlein, H. Becker, B.G. Dietrich, A. Keßler, T. Leibner, G. Wolf, A. Leineweber, U.A. Peuker, H. Biermann, and A. Weidner: *Mater. Charact.*, 2021, vol. 174, p. 111039. <https://doi.org/10.1016/j.matchar.2021.111039>.
16. S. Foss, C.J. Simensen, A. Olsen, and J. Tafto: *Philos. Mag. Lett.*, 2002, vol. 82, pp. 681–86.
17. S. Foss, A. Olsen, C.J. Simensen, and J. Tafto: *Acta Crystallogr. B*, 2003, vol. 59, pp. 36–42.
18. R. Krendelsberger, P. Rogl, A. Leithe-Jasper, and C.J. Simensen: *J. Alloys Compd.*, 1998, vol. 264, pp. 236–39.
19. Q.G. Wang and C.J. Davidson: *J. Mater. Sci.*, 2001, vol. 36, pp. 739–50.
20. Q.G. Wang: *Metall. Mater. Trans. A*, 2003, vol. 34A, pp. 2887–99.
21. J.A. Taylor, D.H. St John, J. Barresi, and M.J. Couper: *Mater. Sci. Forum*, 2000, vol. 331, pp. 277–82.
22. L. Lu and A.K. Dahle: *Metall. Mater. Trans. A*, 2005, vol. 36A, p. 819.
23. J.Y. Yao and J.A. Taylor: *J. Alloys Compd.*, 2012, vol. 519, pp. 60–66.
24. X. Cao and J. Campbell: *Metall. Mater. Trans. A*, 2004, vol. 35A, pp. 1425–35.
25. J. Gan, J. Du, C. Wen, G. Zhang, M. Shi, and Z. Yuan: *Int. J. Met.*, 2021, <https://doi.org/10.1007/s40962-021-00580-0>.
26. S. Viswanathan: *ASM Handbook: Volume 15 Casting*, vol. 15, 2008.
27. S. Terzi, J.A. Taylor, Y.H. Cho, L. Salvo, M. Suéry, E. Boller, and A.K. Dahle: *Acta Mater.*, 2010, vol. 58, pp. 5370–80.
28. C.M. Dinnis, J.A. Taylor, and A.K. Dahle: *Scripta Mater.*, 2005, vol. 53, pp. 955–58.
29. H. Becker, T. Bergh, P.E. Vullum, A. Leineweber, and Y. Li: *Materialia*, 2018, vol. 2, p. 89. <https://doi.org/10.1016/j.mtla.2018.100198>.
30. L. Liu, A.M. Samuel, F.H. Samuel, H.W. Doty, and S. Valtierra: *Int. J. Cast Met. Res.*, 2003, vol. 16, pp. 397–408.
31. F. Mao, G. Yan, Z. Xuan, Z. Cao, and T. Wang: *J. Alloys Compd.*, 2015, vol. 650, pp. 896–906.
32. B. Li, H. Wang, J. Jie, and Z. Wei: *Mater. Des.*, 2011, vol. 32, pp. 1617–22.
33. Y.C. Tsai, C.Y. Chou, S.L. Lee, C.K. Lin, J.C. Lin, and S.W. Lim: *J. Alloys Compd.*, 2009, vol. 487, pp. 157–62.
34. S. Tahamtan, A.F. Boostani, and H. Nazemi: *J. Alloys Compd.*, 2009, vol. 468, pp. 107–14.
35. E. Çadırılı, U. Büyük, S. Engin, and H. Kaya: *J. Alloys Compd.*, 2017, vol. 694, pp. 471–79.
36. J.-O. Andersson, T. Helander, L. Höglund, P. Shi, and B. Sundman: *Calphad*, 2002, vol. 26, pp. 273–312.

**Publisher's Note** Springer Nature remains neutral with regard to jurisdictional claims in published maps and institutional affiliations.